Applied Thermal Engineering 215 (2022) 118949

Contents lists available at ScienceDirect

Applied Thermal Engineering

journal homepage: www.elsevier.com/locate/ate

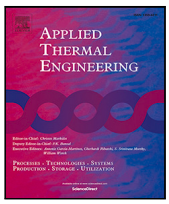

Research Paper

Modeling the external flow of a novel HorseShoe receiver and the evaluation of thermal performance

A. Martín-Alcántara [b], J.J. Serrano-Aguilera [a,*], L. Parras [a]

[a] Universidad de Málaga, Escuela de Ingenierías Industriales, Campus de Teatinos s/n, 29071, Málaga, Spain
[b] AICIA - Thermal Engineering Group, Camino de los Descubrimientos s/n, 41092, Sevilla, Spain

ARTICLE INFO

Keywords:
Parabolic trough collector
CSP
Linear focusing systems
Solar linear cavity receiver
HorseShoe receiver

ABSTRACT

The linear receiver of a Parabolic Trough Collector is the most critical element in the entire system. The Universal Vacuum Air Collector concept is the most extended type of receiver in both experimental and industrial facilities. Besides their considerable cost, their efficiency usually drops as operation time passes. This is mainly due to a partial loss of vacuum in the evacuated annulus between the absorber and the glass cover. An alternative design called HorseShoe receiver is proposed in this work, whose main goal is to maintain the thermal performance throughout its entire lifespan. This innovative receiver is indicated for low-to-medium temperature ranges, which is particularly suitable for solar heat for industrial processes. It consists of a horseshoe-like cavity absorber having its upper border insulated. In addition, two main advantages can be taken by using two symmetric lenses as glass cover: reconcentrate solar radiation into the cavity (improvement of the intercept factor) and protect stratification conditions (reduction of thermal losses). A transient numerical model with customized boundary conditions has been implemented to evaluate both thermal performance and temperature difference in the absorber domain, which is critical for the thermal stress conditions. For that purpose and as a key contribution, not only the Heat Transfer Fluid (HTF) temperature but also the heat transfer coefficient in the duct are set. In particular, HTF temperature ranges from 80 °C to 220 °C and the inner heat transfer coefficient from 600 W/(m^2·K) to 1800 W/(m^2·K). Results show that numerical thermal performance is above 96%, which is mainly due to the reduction of thermal radiation losses, where the absorber active surface emittance is $\epsilon_{abs} = 0.3$. Since no inclination of the receiver has been considered in this initial study, it is shown that the air inside the cavity is stratified, which reduces convective losses. Moreover, temperature difference between the coldest and the hottest spot of the absorber is no higher than 30 K, which is affordable from a technical point of view. A polynomial heat losses correlation is also provided, whose parameters are on the same order of those by conventional receiver correlations available in the literature.

1. Introduction

Environmental implications of global warming have become a significant challenge to face in the coming years. Future energy policies should turn into a sustainable alternative to fossil fuels. As a matter of fact, concentrated Solar Power (CSP) is one of the key elements to achieve that goal, where linear focusing systems show relevant prospects nor only for electricity generation but also to deliver heat for industrial processes. Within this field, Parabolic Trough Collectors (PTCs) are the most spread technology, consisting of a linear receiver which is installed on the focal line of a parabolic reflector. The receiver is the most critical element, since the majority of heat transfer processes take place there. Current PTC systems use the UVAC (Universal Vacuum Air Collector) receiver concept [1], which is essentially formed by a steel made absorber tube with synthetic thermal oil flowing inside as heat transfer fluid (HTF). A glass envelope covers the receivers so that air is removed from the annulus between them (vacuum annulus). It is essential to maintain vacuum conditions to avoid excessive thermal losses. Because of the position and geometry of the parabolic mirror, the bottom half of the absorber receives most of the concentrated radiation causing thermal stress on the tube wall. This type of receiver stands out for being quite efficient from the thermal and optical point of view but after all the experience gained throughout several decades of operation, continuation of this technology is also dependent on some practical problems not usually addressed in literature. Some inherent aspects to the conventional design still make it expensive and less durable than expected. Those practical problems limiting the lifespan of the receivers have a direct impact on the pay off period, and the subsequent increase

* Corresponding author.
E-mail addresses: jj.serragui@uma.es, jj.serragui@gmail.com (J.J. Serrano-Aguilera).

https://doi.org/10.1016/j.applthermaleng.2022.118949
Received 17 December 2021; Received in revised form 11 June 2022; Accepted 3 July 2022
Available online 13 July 2022

in the maintenance costs. The unexpected drop of the receiver thermal performance, or the glass envelope break due to thermal bending can be highlighted. Note that heat collection elements are responsible for a major portion of the direct capital costs [2].

The vacuum annulus is sealed by an expensive glass-to-metal welding at both edges of the receiver. This welding joins the edge of the glass envelope with a metallic bellow which compensates the different thermal expansions of metal and glass tubes. Any flaw or leak in the welding [3] or bellow causes a complete or partial loss of vacuum in the receiver [4], leading to a significant build-up of the convective losses. In addition, due to the working temperatures reached by the HTF, H_2 is generated [5]. The permeation of these molecules through the steel absorber deteriorates the vacuum level. It is a relatively slow process, but it eventually limits the lifespan of receivers regardless of possible failures in the glass-to-metal welding.

Concentrated solar radiation impinges on the outer surface of the metal absorber. Thus, this area reaches the highest temperature in the whole UVAC receiver, emitting thermal radiation outwards, so a high-temperature selective coating is needed to reduce thermal emittance on this surface. Apart from noticeably increasing the cost of receivers, the selective coating tends to reduce their optical properties with time and are not fully stable in air at atmospheric conditions [6]. It seems to be stable during the first four years of operation, but after the first five years, no level of efficiency is officially guaranteed [7]. Moreover, the induced thermal gradient and the subsequent thermal bending can sometimes break the glass cover, which leads to a total failure of the receiver [8].

Due to these reasons, the rate of failure in this type of absorber, which is not negligible, directly affects the O&M costs in PTC power plants along with mirror replacements [9]. Any sort of flaw entails the replacement of the whole receiver. This is particularly critical because the price of the receivers accounts for a relevant share of the total cost of the power plant. Moreover, the gradual decay of the receivers output penalizes the overall system performance as a result of the previous weak spots. The estimated lifetime of PTC plants assumed to calculate LCOE is approximately of 25 years, which is significantly lower than other types of power plants (e.g. nuclear, coal). The lack of fuel costs in solar plants would lead to a drastic reduction in the LCOE of PTC plants as the aging of their components (i.e. receivers and reflectors) is slowed down.

New concepts of linear focusing receivers have been proposed in order to provide solutions for the aforementioned challenges. Some of them do not add substantial modifications to the conventional UVAC concept, such as the HITECO design [10]. It relies on a continuous vacuum annulus spanning several absorber tubes (with the length of a semicolector) by means of dynamic vacuum operation, where vacuum is produced in the solar field during operation. The use of an additional glass envelope has been also suggested and numerically tested [11], showing an improved thermal performance. Alternatively, the gap between the absorber and the glass of conventional UVAC receivers can be filled with different types of gas [12], which have an effect on thermal losses. Moreover, Patil et al. [13] suggested to insulate the top half of the absorber by filling part of the annulus (half insulation-filled receiver) or by replacing a relevant fraction of the perimeter of the glass cover with an insulation. Recently, El-Bakry and co-authors [14] proposed that a heat shield with a 75 mm diameter and 150° shading angle performs the best.

Cavity receivers are common in point-focus systems: this is the case of parabolic dishes [15,16], which can also take advantage of a glass cover and secondary reflectors [17,18] as well as in tower receivers [19]. In line with this, the concept of cavity can be incorporated to line focusing systems, leading to linear cavity receivers, which substantially differ the UVAC concept. Despite showing interesting prospects, no many studies can be found in the literature about it: one of the first versions was proposed by Barra et al. [20]. They described what they named as Black Body receiver used to produce renewable heat for a brewery. The receiver consisted of an arch-like metal piece along with a V-shaped lid of pyrex glass. It works as a linear cavity containing several copper pipes inside. Moreover, a triangular cavity receiver was proposed by Rafiei at al. [21] later on. A flat glass cover closed the triangle base (facing to the reflector), whereas a set of small tubes are installed on the two remaining faces of the triangle. A triangle cavity absorber was also suggested by Zhai et al. [22] in a hybrid solar heating and cooling system. An analogous variant (but this time based on a rectangular cavity) was proposed in the study by Loni et al. [23], where the optimal position of the cavity as well as its size were sought. All of the aforementioned cases, have shown cylindrical ducts for the HTF, however, as described by several authors [24,25], this geometry can be substantially modified to increase the heat transfer area between the metal absorber and the HTF. This is also the case of the lunate channel design proposed by Li et al. [26]. This work evaluates the thermal performance of a novel receiver whose absorber relatively resembles the lunate channel, but with additional optical elements improving both the optical and thermal efficiency, unlike the present study, the aforementioned work does not consider the effect of the duct heat transfer coefficient in the thermal losses. Despite not using an optimized definitive metal absorber geometry, the goal of the present study is to evaluate thermal losses of the cavity given a prescribed slit width d along with the lenses. In addition, the development and setup of a numerical tool predicting the performance of solar receivers is a key contribution of this work. Therefore, thermal boundary conditions are set in such a way that thermal gradients concerning metal absorber can be evaluated.

Table 1
Parameters defining the geometry of the receiver.

Geometric parameters	
d	0.060 m
A_w	0.085 m
A_h	0.120 m
C_w	0.021 m
l_s	0.062 m
l_h	0.105 m
l_w	0.161 m
I_h	0.040 m

2. Description of the open HorseShoe receiver

The open version of the HorseShoe receiver is engineered for medium to low temperature range (i.e. from 90 to 200 °C), fitting many applications for industrial process heat. A more detailed description of the system as well as some configuration details can be found in the document of the already accepted patent.[1] The particular geometry of the receiver is defined in the aforementioned document and it is the result of an optimization process based on an in-house Monte Carlo Ray-Tracing model developed in previous works [27,28]. The two symmetric lenses (also known as covers, see Fig. 1) have dual function: redirecting the most crosswise rays to improve the intercept factor and protecting the region of stratified air to limit convective losses. Instead of using an integral glass cover with this open configuration, only crosswise rays have to go trough the lenses. The rays coming from the central region of the reflector go directly onto the absorber without being affected by any sort of optical loss due to refraction, reflection and the Beer–Lambert absorption.

The duct, where heat is collected by the HTF, is surrounded by the metal absorber (depicted in black color in Fig. 1). An outer thermal insulator (i.e. mineral wool) prevents from any sort of thermal loss through the upper border of the absorber. The aperture of the slit

[1] International patent application WO2021148701A1 and Spanish patent ES2844999B2.

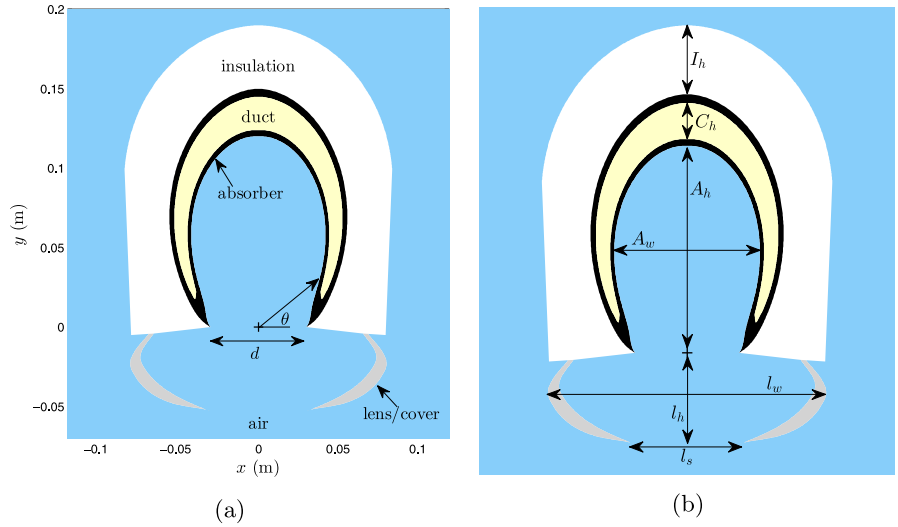

Fig. 1. Diagram of the HorseShoe receiver: (a) Focal point of the reflector + is located at the origin of the coordinate system. (b) Graphical description of the main geometric parameters.

through which concentrated radiation enters into the cavity ($d = 0.06$ m), is a characteristic length of the receiver design since it is proportional to radiative and convective losses. It is the most critical parameter, which is the result of the trade-off between the optical intercept factor and thermal losses. The inner wall of the metal absorber (surface in contact with air) has been designed so that no significant azimuthal gradients of concentrated solar flux take place in that face of the absorber. A selective coating is also recommended for that interface, but optical features (particularly the thermal emittance, ϵ_{abs}) is not as critical as in the conventional design since d is less than $1/3$ of the perimeter of a conventional LS3 absorber, with the subsequent reduction in the thermal radiation losses. Note that this is the case, because the outer diameter of a LS3 absorber ($d_{LS3} \approx 0.07$ m) is bigger than $d = 0.06$ m. The cross sectional area of the duct is analogous to the LS3 absorber case but taking advantage of a higher wet perimeter.

The reflector is defined by a continuous profile composed of two regions (see Fig. 2). The central region $x \in [-x_{trans}, x_{trans}]$ is a pure parabolic mirror with a characteristic focal distance f_{mod}. However, the outer region of the reflector $x \in [-W_{LS3}, -x_{trans}] \bigcup [x_{trans}, W_{LS3}]$ is the solution of the next ordinary differential equation, which depends on two parameters, δ and a:

$$\frac{dy}{dx} = \tan\left[\frac{\pi}{4} + \frac{\delta}{2} + \frac{1}{2}\arctan\left(\frac{y}{x-a}\right)\right], \tag{1}$$

where the origin of the coordinate system is located at the focal point. Note that δ is an angle which must be on the order of the subtended solar disk semiangle and a can be set as $d/2$. The particular design used in this study (modified profile) is displayed in Fig. 2 in comparison with the classic LS3 reflector geometry. Both reflectors have the same aperture width, so the solar radiation input is equivalent. Table 2 shows the parameter values assumed for the particular modified reflector geometry used in this study. Its arc length is 3.15% shorter than the LS3 design. This entails a cost reduction due to reflective materials because the reflective area is cut down in the same proportion.

The combination of the reflector and the open symmetric lenses concentrates solar radiation according to a specific heat flux pattern on the inner face of the metal absorber, spanned by the angle $\theta \in [0, \pi]$ (see Fig. 1). It has been defined in terms of the Local Concentration Ratio (LCR) as displayed in Fig. 3. This distribution is essential to set the thermal boundary conditions on the inner face of the absorber.

The described linear cavity collector is based on the combination of the receiver alongside the reflector. It has been defined this way so that, despite setting a narrow slit (low value of d), the intercept factor is higher than 97%. The geometric description of the particular receiver considered in this study has been defined in Fig. 1(b) along the values assigned to the characteristic lengths displayed in Table 1. This whole design takes advantage of the ascending nature of buoyancy-driven flow, which enables stratification of the air inside of the open chamber delimited by the absorber and the lenses. Note that the top part of the cavity is at higher temperature. Therefore, the protection provided by the lenses at both sides, allows that buoyancy-driven forces lead to a virtually stagnant flow due to the air temperature gradient in the vertical direction. This receiver provides several technical advantages since it lacks of the most vulnerable elements of the traditional UVAC absorber (e.g. glass-to-metal welding and expansion bellows), leading to a robust receiver which keeps stable thermal performance throughout his entire lifespan. Due to the fact that it is formed by three independent elements (insulation, absorber and lenses), in-site repair is possible in case of failure of any of the elements without having to replace the whole receiver. It also eases instrumentation tasks: as a consequence of the insulation layer in the upper border of the absorber, this metal wall is virtually at the same temperature as the HTF. It means that this temperature can be measured without having to drill the absorber wall. Finally, it is relevant to point out that in further designs, absorber geometry can be modified (provided that d does not substantially change) to increase the heat transfer area with the HTF. It lets to reduce thermal gradients taking place in the absorber or having acceptable heat transfer rates at low HTF mass flow rates. The particular design considered in this study is defined in further detail in Fig. 1(b).

The objective of this work is to evaluate the feasibility of the HorseShoe design regarding the most relevant heat transfer mechanisms in terms of the thermal losses: convection and thermal radiation. For this reason, the model to be described in Section 3 does not analyze (i) optical losses or (ii) volumetric absorption of solar radiation within the glass cover, which barely affects thermal efficiency. In this first study, neither the (iii) influence of the inclination of the receiver nor (iv) thermal losses through the support brackets have been accounted. Moreover, (v) lenses and thermal insulation have been assumed as adiabatic. Since this study relies on a 2D model, (vi) no 3D effects have been considered (i.e. 3D nature of the thermal plumes and insulation at the end of the receiver). In addition, the (vii) thermal transport properties of the solid absorber have been set as constant due to the limited variation of thermal conductivity for the existing temperature distribution. Due to the nature of the buoyancy-driven forces, such simplifications can be assumed in order to test whether the thermal stratification in the receiver cavity is effective, which is the essential condition that must be fulfilled to prove the potential of the design.

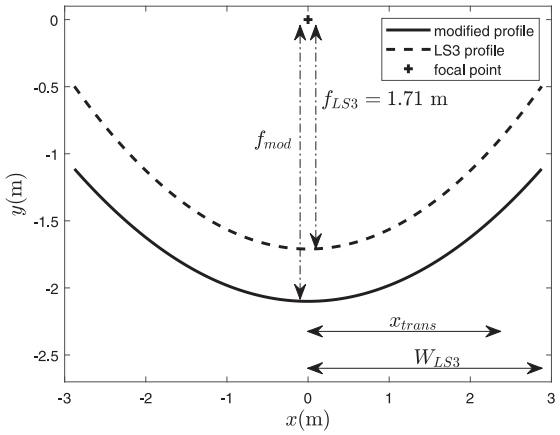

Fig. 2. Modified reflector profile in comparison with the LS3 reflector profile as reference.

Table 2
Parameters defining the modified geometry of the reflector.

Parameter	
f_{mod}	2.1 m
a	0.03 m
W_{LS3}	5.76/2 m
x_{trans}	2.4 m
δ	5.5 mrad

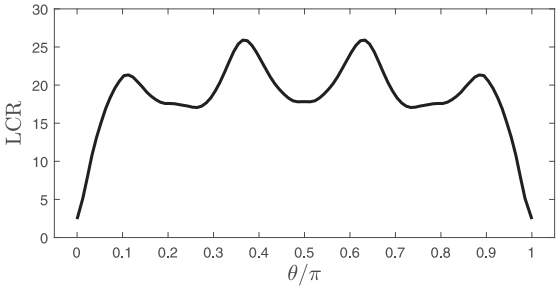

Fig. 3. Local Concentration Ratio (LCR) distribution on the irradiated absorber surface. The definition of θ can be seen in Fig. 1.

3. Numerical model and governing equations

A customized tool has been developed to solve numerically mass, momentum and energy conservation Eqs. (2)–(5) by using the `cht-MultiRegionFoam` solver in the finite volume framework OpenFOAM® [29]. In this problem, the solver is configured to account for the solution of a transient, compressible fluid flow (perfect gas) and solid heat conduction with conjugate heat transfer between regions.

$$\frac{\partial \rho}{\partial t} + \nabla \cdot (\rho \mathbf{v}) = 0, \tag{2}$$

$$\frac{\partial}{\partial t}(\rho \mathbf{v}) + \nabla \cdot (\rho \mathbf{v}\mathbf{v}) = -\nabla p + \nabla \cdot \tau - \rho \mathbf{g}, \tag{3}$$

$$\frac{\partial}{\partial t}(\rho e) + \nabla \cdot (\rho \mathbf{v} e) + \frac{\partial}{\partial t}(\rho K) + \nabla \cdot (\rho \mathbf{v} K) + \nabla \cdot (\mathbf{v} p) = -\nabla \cdot \mathbf{q} + \nabla \cdot (\tau \cdot \mathbf{v}) + \rho r + \rho \mathbf{v} \cdot \mathbf{g}, \tag{4}$$

where

$$\tau = \mu \left[\nabla \mathbf{v} + \nabla \mathbf{v}^T - \frac{2}{3} \nabla \cdot \mathbf{v} I \right]. \tag{5}$$

In the above equations, ρ is the density, μ is the viscosity, τ is the viscous stress tensor, t is time, $\mathbf{v}$ is the velocity vector, and p is the pressure. The energy equation is solved in terms of sensible internal energy e, with $K = v^2/2$, α and r, the kinetic energy, the thermal diffusivity, and an additional heat flux, respectively. In the present study, r stands for the radiation effects which were considered through the View Factor model (see Section 3.1), as heat source acting on the fluid–solid wall (see Σ_4 in Fig. 4 and Table 3).

Alternatively, only the heat diffusion is solved in the solid region, i.e.

$$\frac{\partial}{\partial t}(\rho h) = \nabla \cdot (\alpha \nabla h), \tag{6}$$

h being the enthalpy.

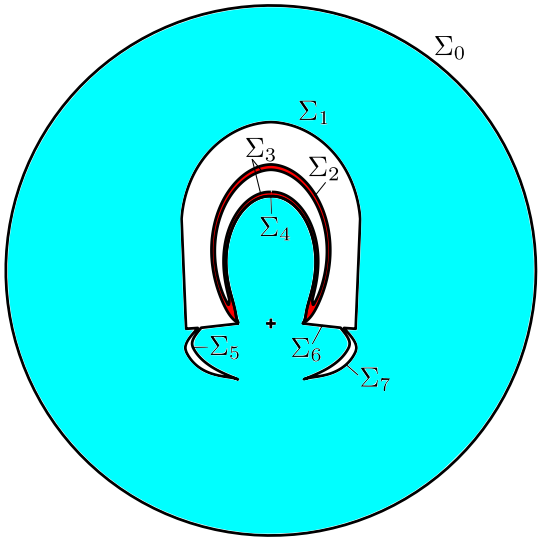

Fig. 4. Schematic of the patches defined in the computational domain. In blue fluid region, and in red solid.

Table 3
Boundary conditions applied on the fluid and the solid regions.

	T K	$\mathbf{v}$ m/s	p Pa	q W/m^2	q_{src} W/m^2
Σ_0	$\mathbf{n} \cdot \nabla T = 0$	$\mathbf{n} \cdot \nabla \mathbf{v} = 0$	101 325	–	q_{rad}
Σ_1	$\mathbf{n} \cdot \nabla T = 0$	0	$\mathbf{n} \cdot \nabla p = 0$	–	–
Σ_2	$\mathbf{n} \cdot \nabla T = 0$	–	–	–	–
Σ_3	–	–	–	$q_s = h_f A (T_f - T_s)$	–
Σ_4	$T_f = T_s$	0	$\mathbf{n} \cdot \nabla p = 0$	$q_f = -q_s$	$q_{sun}(\theta) + q_{rad}$
Σ_5	$\mathbf{n} \cdot \nabla T = 0$	0	$\mathbf{n} \cdot \nabla p = 0$	–	q_{rad}
Σ_6	$\mathbf{n} \cdot \nabla T = 0$	0	$\mathbf{n} \cdot \nabla p = 0$	–	q_{rad}
Σ_7	$\mathbf{n} \cdot \nabla T = 0$	0	$\mathbf{n} \cdot \nabla p = 0$	–	–

3.1. Thermal radiation

Besides the governing equations for both fluid and solid domains, heat exchange due to thermal radiation should be taken into account. Differential surfaces from the patches Σ_0, Σ_4, Σ_5 and Σ_6 have been assumed as gray diffusive surfaces (see Fig. 4). In order to obtain the net heat flux due to thermal radiation in any differential surfaces, a linear algebraic system has to be solved [30]:

$$\underbrace{\left[\frac{\delta_{ij}}{\epsilon_j} - \left(\frac{1}{\epsilon_j} - 1 \right) F_{i-j} \right]}_{\mathbf{C}_{N \times N}} q_{rad,j} = \underbrace{\left[\delta_{ij} - F_{i-j} \right] \sigma T_j^4}_{\mathbf{B}_{N \times 1}}, \tag{7}$$

where the solution $q_{rad,j}$ is a $N \times 1$ column vector containing the individual heat flux terms for any of the N differential surfaces. Note that i, j stand for the indexes of the elements in the linear system, δ_{ij} is the Kronecker delta operator and F_{i-j} indicates the view factor of any pair of differential surfaces. Constant emittance $\epsilon_j = \epsilon_{abs}$ corresponds to those surfaces belonging to Σ_4, whereas the emittance of the remaining

surfaces is $\epsilon_j = \epsilon_{surr}$. The Stefan–Boltzmann constant σ along with the individual temperature of patches T_j complete the already-known elements for any iteration.

3.2. Boundary conditions

The Eqs. (2)–(6) were solved by applying the following boundary conditions on the respective patches (see Fig. 4). Special attention should be paid to the boundary conditions corresponding to the walls of the duct (Σ_3): A representative temperature of the HTF inside the duct is prescribed T_f along with the heat transfer coefficient inside h_f (see Table 3). The incoming heat to the solid q_s (which is at temperature T_s) also depends on the area of heat exchange A between the fluid and the wet perimeter of the absorber. The second patch with a special boundary condition is on the fluid–solid wall (Σ_4). Numerically, it is implemented by using two neighbor layers (one on the fluid region and the other on the solid) interacting one with each other such that both the temperature and the heat flux are continuous, as described in Table 3. For the sake of clarity, it is worth mentioning that from a physical perspective, Σ_3 consists of one single wall, only a boundary condition (with the aforementioned working strategy) being prescribed. Additionally, an external heat source $q_{sun}(\theta)$ coming from the solar concentrated radiation distribution by the mirror and the lenses (see Fig. 3) is injected on the domain. Since this source term is a function the θ angle, it was implemented in such a way that its value is interpolated on each cell face of Σ_4 from a lookup table (the `interpolationTable.H` class was used for this purpose). Radiation is also enabled to act on this boundary through the radiative source term q_{rad}.

As initial conditions, the air was set initially at rest and at $T_f = 300$ K in the entire computational domain. In order to avoid excessive transient computing period, the initial temperature in the solid domain was related to T_f.

3.3. Numerical settings

The conjugate heat transfer problem is solved numerically by using a customized version of the `chtMultiRegionFoam`, included in the OpenFOAM® v2012 [31]. This solver combines the heat transfer between several fluids and/or solids by solving the appropriate conservation Eqs. (2)–(6) with the specific boundary conditions (see Table 3) accounting for the heat exchange. It is worth mentioning that some of the boundary conditions in Section 3.2 are nondefault and were accordingly implemented for the development of this tool. Some recent works [32–34] validated and showed the ability of the code to solve this kind of problems.

The temporal integration of the problem is carried out by following a second order, Crank–Nicolson scheme, with a time marching ensuring $\max\{\text{CFL}\} = 0.99$ is achieved in each time step over the entire domain. Such nondimensional condition relating the grid length with the convective velocity ($\text{CFL} = u\Delta t/\Delta x$) is intended for the stability of the explicit terms used in the numerical discretization. The restriction CFL < 1 basically represents that a fluid particle cannot move more than one grid length in a single time step. For the spatial discretization, second order stencils are adopted with a proper Gaussian quadrature rule. The `PIMPLE` algorithm was used to deal with the pressure–velocity coupling in the momentum equation. This algorithm blends the `SIMPLE` and the `PISO` capabilities [35], introducing both outer and inner loops. If a residual control is used for the outer loop, the convergence of the solver can be improved substantially, it being possible to even reach CFL > 1 if stable.

A grid sensitivity study on the total heat loss Q_{total} was carried out in three consecutive refined meshes, each with approximately twice as many elements as the previous one. Table 4 exhibits the results indicating that the grid #2 is the most suitable to be used according to the relative error (ε_n^{n+1}) and the equivalent computational cost between two adjacent meshes.

Table 4
Grid sensitivity study.

	Number of elements	Q_{total} W/m	ε_n^{n+1}	Speed up respect to grid #2
Grid #0	35 678	143.0775	–	32.87
Grid #1	74 360	143.2424	0.1151%	14.28
Grid #2	168 468	143.2113	0.0217%	1.00

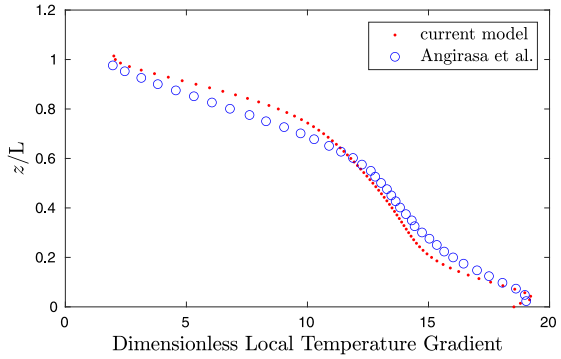

Fig. 5. Spatial evolution of the dimensionless local temperature gradient on the normal direction to the hot wall. Validation comparing the numerical results by the current model with those provided by Angirasa et al. [41] in a square cavity open on one side at $Gr = 10^6$.

3.4. Model validation

The numerical solver `chtMultiRegionFoam` has been successfully validated in the literature against experimental results in buoyancy-driven flow problems with air. This is the case of the differentially-heated cavity problem [36]. It has also been validated in some engineering applications, such as heat sinks cooled by air [37] and battery cooling [38], the effectiveness analysis of a fin [39] or applied in classic heat transfer problems, like the conjugated heat transfer between a spherical particle rolling over a planar surface [40] or the conjugate heat transfer in a 3D rectangular duct [32].

The innovative nature of the HorseShoe receiver makes it difficult to carry out an experimental validation of the proposed design so far. Since no experimental data is available for the HorseShoe receiver, a direct validation is not currently possible. However, buoyancy-driven model in which the `chtMultiRegionFoam` solver is based on, has been compared with numerical and experimental results of a two-dimensional square open cavity. This classic problem is a suitable reference since it reproduces diffusive and convective thermal losses due to air buoyancy at atmospheric conditions and it also resembles the current design in term of geometric proportions. In the numerical study by Angirasa et al. [41] a square cavity open on one side is solved by means of the Boussinesq approximation for a Newtonian fluid at $Pr = 0.7$ and $Gr = 10^6$, where the Grashof number is defined in Eq. (8), β represents the air thermal expansion coefficient and L the side length of the square cavity,

$$Gr = \frac{\rho^2\ g\beta(T_w - T_{amb})L^3}{\mu^2}. \tag{8}$$

Since the two horizontal walls are adiabatic and the vertical wall is heated at constant temperature T_w, Fig. 5 [41] shows the evolution of the dimensionless local temperature gradient in the normal direction with respect to the hot surface along the hot wall z/L. The current model provides similar results to those by Angirasa et al. with a similar trend despite using a compressible fluid model.

Not only numerical, but also experimental results have been used for comparison. Sernas & Kyriakides [42,43] tested the same geometry to measure the local heat transfer coefficient h_l for air ($Pr = 0.7$) at $Gr = 10^7$. As displayed in Fig. 6, experimental results fit those provided

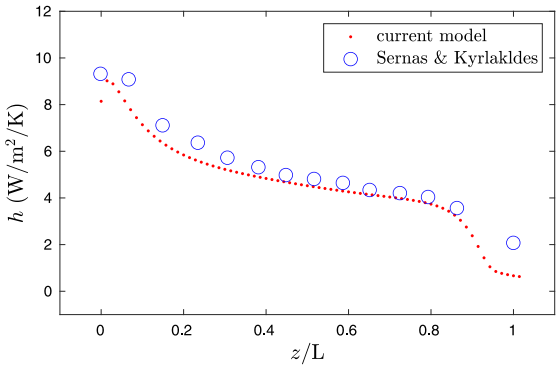

Fig. 6. Spatial evolution of the local heat transfer coefficient of the hot wall in a square cavity open on one side for $Gr = 10^7$. Validation comparing the numerical results by the current model with the experimental values provided by Sernas & Kyriakides [42,43].

by the current model. The difference found at $z/L > 0.9$ can be explained due to the fact that, unlike the current model used in this validation, the top horizontal wall in the experimental setup by Sernas & Kyriakides was not fully adiabatic.

Moreover, despite consisting on averaged values, the experimental results provided by Chakroun et al. [44] are also of interest because they have tested downward-facing cavities. Regardless the cavity width/height aspect ratio, averaged Nusselt number is on the order of $Nu \sim 1$ for downward-facing cavities. It makes sense, since thermal diffusion is also a relevant heat transfer mechanism in fully stratified cavities. In order to validate our model in this particular case, a square cavity for $T_w = 79$ °C and $L = 0.1485$ m, has been selected. The average Nusselt number obtained by the current model is $Nu = 1.94$ which is close to the experimental value provided by Chakroun et al. [44] $Nu = 1.91$ and within the 5.45% margin error due to the experimental uncertainties.

In addition, when regarding CSP applications, the current model have been compared with the experimental characterization of a PTR-70-DSG UVAC receiver (see Section 4.3). Despite consisting of different concepts of receivers, the two-parameter fitting of the total heat losses by the current model is similar to the PTR-70-DSG correlation. All these facts allow us to conclude that the current CFD code is capable of reproducing the dependency between the aforementioned heat losses and the absorber mean temperature.

4. Results

Due to the unstable nature of the thermal plume (see Fig. 7) responsible for the convective heat losses, a transient solver has been used. Transient simulations have been run until steady conditions are reached in the metal absorber domain, for every case tested. Once those conditions have been achieved, averaged quantities can be used to describe the heat losses leaving from the inner face of the absorber (Σ_4).

Results from all the tested cases follow the same pattern. As depicted in Fig. 8(a), temperature distribution indicates that the air inside the receiver is strongly stratified. Temperature inside the main/upper cavity (surrounded by the metal absorber) is almost uniform, whereas the secondary cavity (bottom cavity delimited by the symmetric lenses) protects the stratification of the main cavity due to the vertical temperature gradient. According to Fig. 8(b), it has been found a buoyant flow which leaves upwards from the receiver, alternating from side to side (see videos in supplementary material for further details). Convective losses are limited because the temperature of the buoyant flow is barely hotter than the ambient temperature (note that the color scale saturates at $T = 303$ K). In accordance with the previous description, Fig. 8(c) shows that the magnitude of the velocity field is particularly

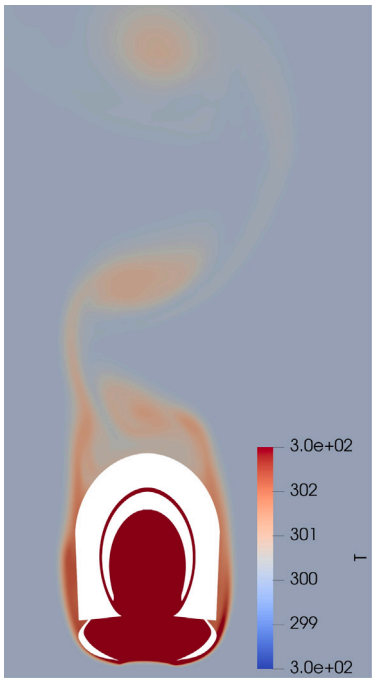

Fig. 7. Temperature field of the domain with modified scale color where $T > 303$ K is saturated in red color. Thermal plume leaving upwards from the receiver.

higher at both sides of the receiver, where the plumes departs from. In addition, the temperature distribution of the absorber wall is displayed in Fig. 8(d), where the outer wall is virtually at the same temperature as the HTF (T_f), but in contrast the inner wall is at considerable higher temperature. This inner wall is the active one, which transfers the incoming heat flux to the duct. Temperature is particularly hot at both peaks of the HorseShoe, which entails some future changes in the absorber design. This issue could be relevant at the time of evaluating the risk of mechanical failure after a specific number of cycles as a result of the subsequent thermal stress.

4.1. Evaluation of total thermal losses and temperature difference

A set of 56 (7 × 8) numerical experiments have been carried out in order, not only to evaluate the total heat losses of the receiver (Q_{total}), but also the temperature difference within the absorber domain. The latter turns out to be a critical factor to evaluate the feasibility of the proposed design because such difference between the hottest and coldest part of the metal absorber is limited in order to guarantee the system functionality. For that purpose two operation parameters have been considered. Firstly, the temperature of the fluid circulating inside the duct T_f is the key parameter that conditions the absorber temperature, which in turns affects the thermal losses. Secondly, the heat transfer between the HTF and the absorber due to forced convection can be modeled by means of the heat transfer coefficient inside the duct h_f. It essentially depends on the flow conditions (i.e. Re number, rugosity and thermophysical properties). Simulation conditions are detailed in Table 5, where the 56 pair of values in the $T_f - h_f$ space are defined. Constant emittance ϵ_{abs} in the inner face of the absorber (Σ_4) is used as well as the remaining surfaces exchanging thermal radiation show a higher value ϵ_{surr}. The total heat losses have been calculated from the solar–air interface (Σ_4) as detailed in Eq. (9), where q_f is the normal-to-surface heat flux transferred from the lower solid border to the surrounding air and q_{rad} represents the net thermal radiation leaving Σ_4,

$$Q_{total} = \int_{\Sigma_4} q_f \, ds + \int_{\Sigma_4} q_{rad} \, ds. \tag{9}$$

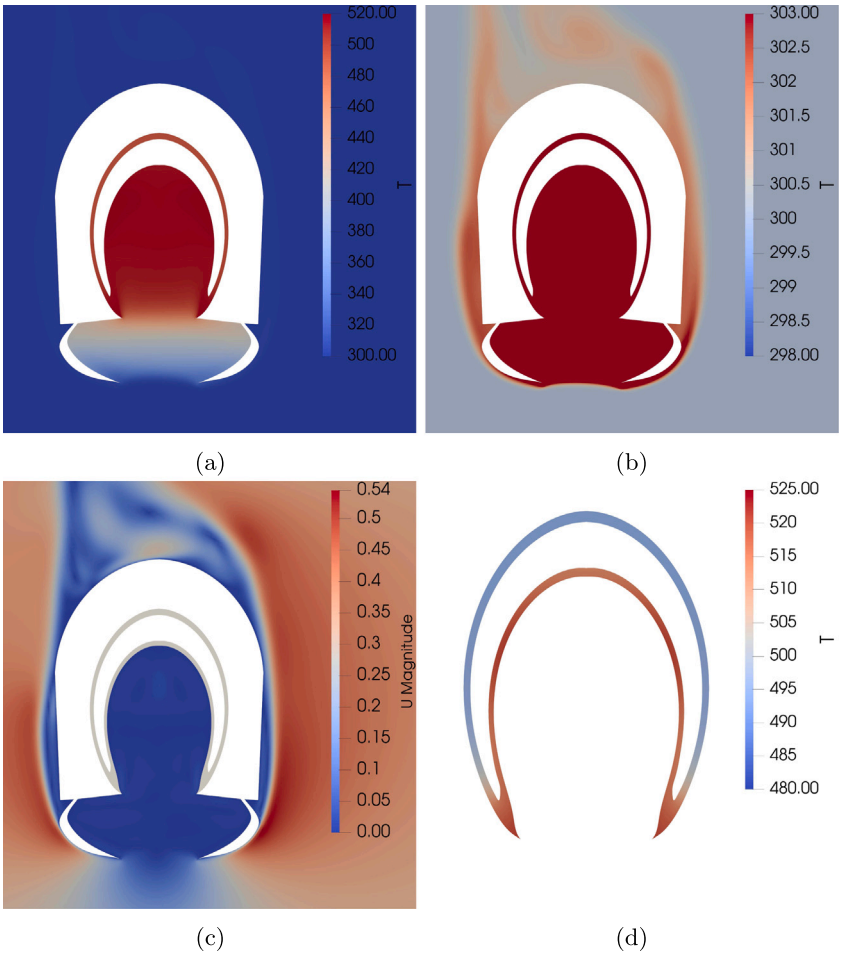

Fig. 8. Solution for $h_f = 600$ W/(m^2 K) and $T_f = 220$ °C: (a) Temperature distribution of the air surrounding the receiver. (b) Temperature distribution of the air surrounding the receiver with a modified color scale: red color saturates when $T > 303$ K. (c) Magnitude of the velocity field due to buoyancy-driven flow. (d) Temperature distribution of the metal absorber wall.

The definition of the thermal performance relies on the definition of Q_{total}, since $\eta_{thermal}$ accounts for the fraction of the incoming solar concentrated energy reaching the absorber active surface Σ_4, which is not lost as Q_{total} to the surroundings:

$$\eta_{thermal} = \frac{\int_{\Sigma_4} q_{sun} ds - Q_{total}}{\int_{\Sigma_4} q_{sun} ds}. \tag{10}$$

The thermophysical properties of the absorber material are also set constant: thermal conductivity κ_{abs}, density ρ_{abs} and specific heat capacity $c_{p,abs}$.

Following the LCR distribution displayed in Fig. 3, the mirror reflectance and the solar irradiance (also defined in Table 5), it is possible to determine the concentrated solar heat flux distribution on the inner face of the absorber (Σ_4). As a result of specifying both, the HTF temperature as well as the input concentrated radiation, a realistic temperature distribution of the absorber wall can be provided. Note that in the HorseShoe receiver the wet perimeter is significantly longer than in a conventional absorber. Besides, around 50% of this perimeter (non-active absorber wall bordering the thermal insulation) is virtually at the HTF temperature, which boosts the thermal stress on the absorber domain.

As displayed in Fig. 9 total heat losses are affected by both operation parameters: HTF temperature T_f and the duct heat transfer coefficient h_f. As expected, according to Fig. 9(a), higher values of T_f lead to higher total thermal losses, which accounts for both convective and radiation losses. Similarly to the existing correlations for conventional receivers, a polynomial tendency is reported. The heat transfer coefficient also plays a relevant role on the thermal losses. Given any particular HTF temperature, the higher h_f is, the lower thermal losses are reported. This influence is shown in a greater detail in Fig. 9(b), where this effect is particularly more significant when $h_f < 1400$ W/(m^2 K). The heat transfer coefficient barely affects thermal losses when it exceeds 1400 W/(m^2 K), which means that there is no point in increasing HTF mass flow rate beyond this point. This is because higher pumping power would not lead to any significant thermal performance

Table 5
Operation conditions and design of experiments.

Parameter	
T_f	80, 100, 120, …220 °C (8 values)
h_f	600, 800, 1000, …1800 W/(m^2 K) (7 values)
T_{amb}	25 °C
ϵ_{abs}	0.3
ϵ_{surr}	0.9
κ_{abs} (Carbon Steel)	48 W/(m K)
ρ_{abs}	7833 kg/m^3
$c_{p,abs}$	465 J/(kg K)
Air EOS	Perfect gas: $c_v = 730.91$ J/(kg K)
μ_{air}	$23.8 \cdot 10^{-6}$ Pa s
Pr	0.7
Mirror reflectance	0.87
Irradiance (DNI)	850 W/m^2

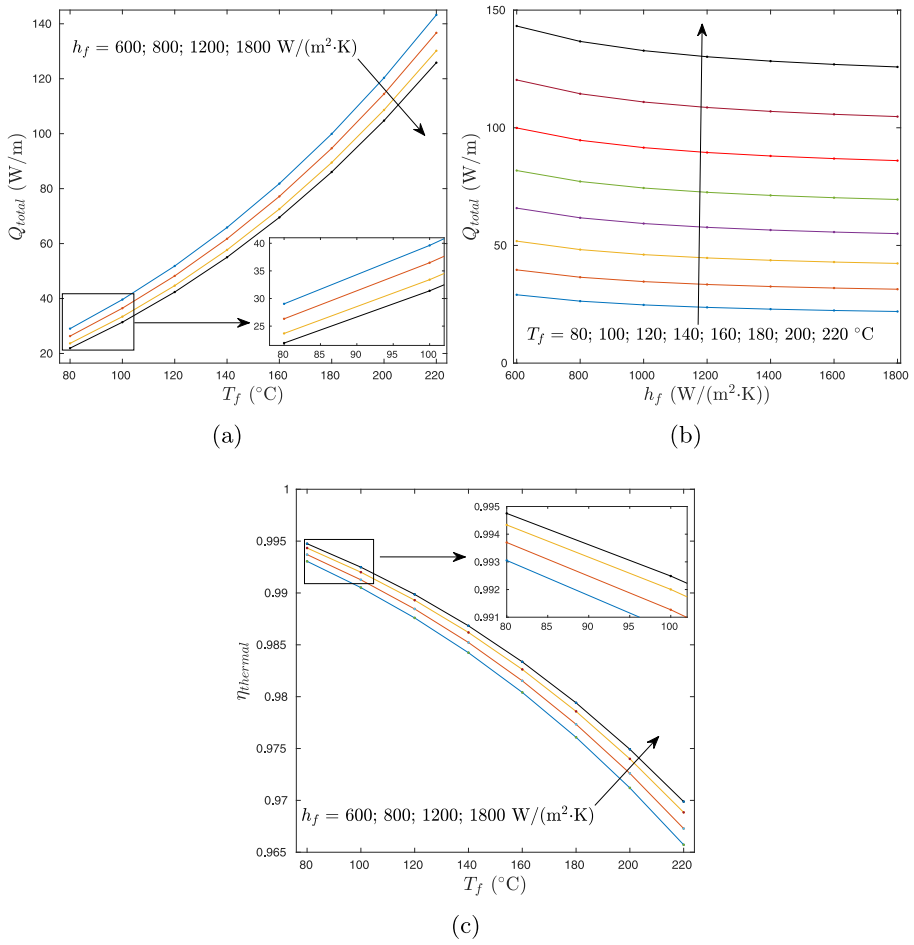

Fig. 9. Evolution of the receiver total heat loss Q_{total}: (a) Dependence on the HTF temperature, T_f, for different heat transfer coefficients in the duct h_f. (b) Dependence on the heat transfer coefficients in the duct for different values of HTF temperature. (c) Global thermal performance $\eta_{thermal}$ as a function of the HTF temperature for several values of the duct heat transfer coefficient.

enhancement, which is depicted in Fig. 9(c). As previously mentioned, thermal performance $\eta_{thermal}$ curves approach to the same limit. Note that, as displayed in that figure, curves tend to overlap as h_f increases.

Thermal performance $\eta_{thermal}$ stands for the fraction of the input power (concentrated solar radiation reaching the lower face of the absorber) which is finally collected by the HTF, so it includes convective and thermal radiation losses. It means that optical losses are not included. According to the numerical results, it can be definitely concluded that most of the thermal losses are due to thermal radiation. It can be explained by the orientation of the absorber, which is the most convenient in terms of convective losses[2] because it allows air stratification. As seen in Fig. 10, the thermal radiation factor ξ_{rad} indicates which fraction of the total thermal losses are due to thermal radiation. This fraction increases when the HTF temperature goes up. At the same time, lower values of h_f lead to a higher fraction of thermal radiation losses.

The temperature difference between the hottest and coldest spot in the metal absorber domain ($T_{abs,max} - T_{abs,min}$) has also been evaluated. As displayed in Fig. 11(a), the HTF temperature hardly conditions the temperature difference. However, the heat transfer coefficient in the duct plays a key role in the absorber thermal stress (see Fig. 11(b)). The external thermal insulation allows adiabatic thermal conditions in the outer border of the absorber, therefore the temperature in the non-active perimeter of the absorber is virtually the same as the HTF temperature. In contrast, a significant temperature difference between the inner wall of the absorber and the HTF exists. It exclusively depends

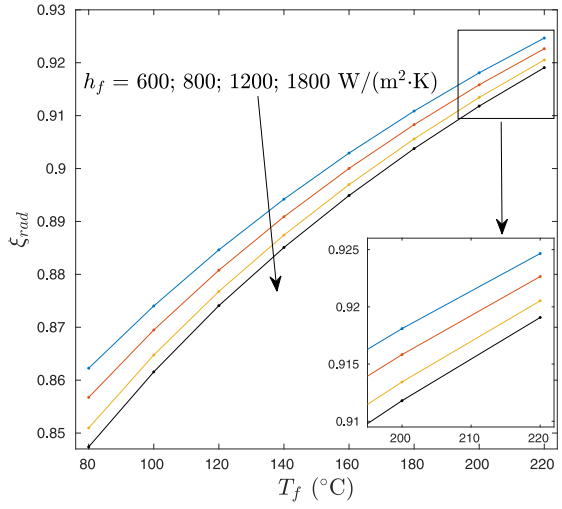

Fig. 10. Fraction of the total heat losses due to thermal radiation (ξ_{rad}) as a function of the HTF temperature T_f for different values of the duct heat transfer coefficient h_f.

[2] By using the term *convective losses* authors mean the combination of diffusive (conduction) along with convective transport through the fluid domain.

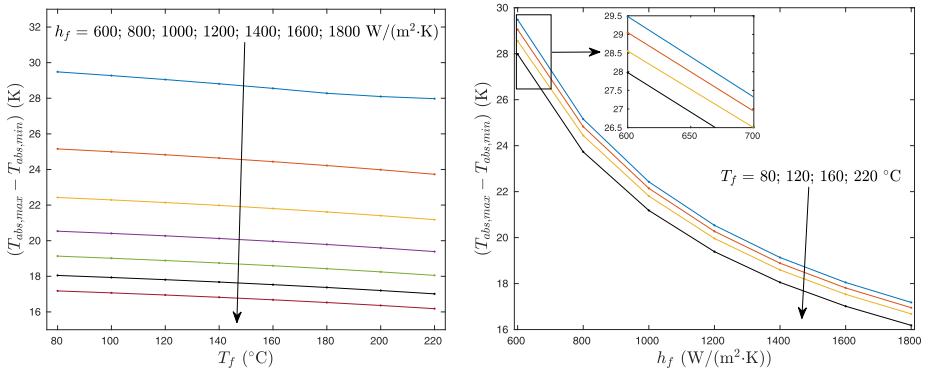

Fig. 11. Temperature difference between the hottest spot and the coldest point of the absorber domain ($T_{abs,max} - T_{abs,min}$) as a function of: (a) HTF temperature T_f and (b) duct heat transfer coefficient h_f.

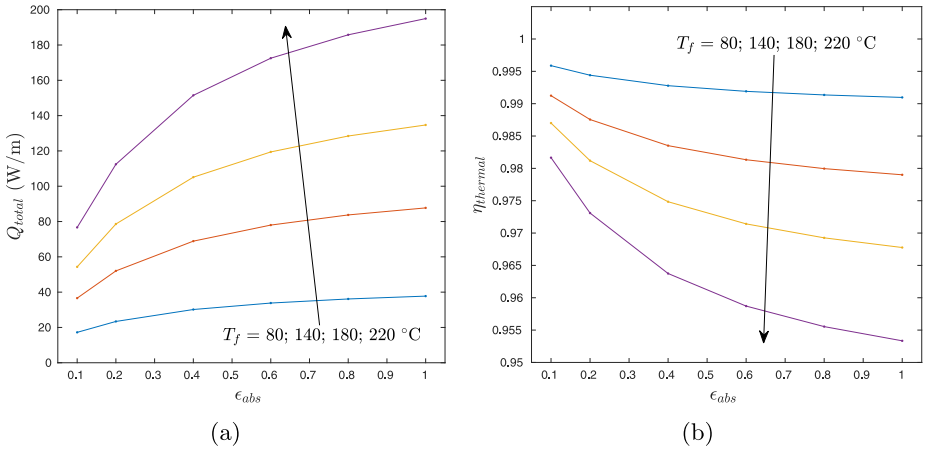

Fig. 12. Effect of the emittance on the inner face of the absorber (ϵ_{abs}) for several values of the HTF temperature T_f given a fixed heat transfer coefficient h_f = 1000 (W/(m² K)) in the duct: (a) Total heat losses Q_{total} and (b) thermal performance ($\eta_{thermal}$).

on the HTF flow conditions and therefore, h_f have a strong influence on it. According to Fig. 11(b), the temperature difference follows a polynomial decay with h_f. Unlike the relationship between Q_{total} and h_f, the temperature difference also depends on the heat transfer coefficient even if $h_f > 1400$ W/(m² K).

4.2. Effect of the absorber emittance on the thermal losses

As previously indicated, given this configuration and the position of the receiver, radiative losses are the most relevant. For this reason, the effect of the emittance on the inner face of the absorber (ϵ_{abs}) has been studied. Unlike in Section 4.1, where a constant $\epsilon_{abs} = 0.3$ value was set, in this case $\epsilon_{abs} = 0.1, 0.2, 0.3, \ldots, 1$ were tested. Besides, the heat transfer coefficient has been set constant $h_f = 1000$ W/(m² K). The dependence of total heat losses and the absorber emittance for several HTF temperatures T_f has been shown in Fig. 12(a). The analogous plot for the thermal performance $\eta_{thermal}$ is provided in Fig. 12(b). The effect of the emittance is negligible when the HTF temperature is low enough (i.e. $T_f = 80°$ C). This is due to the fact that the temperature difference between the absorber (Σ_4) and the surrounding elements of the absorber (Σ_0, Σ_5 and Σ_6) are relatively close. In contrast, as long as the HTF operates at higher temperature, this difference is more significant, leading to a sharp increase of the thermal radiation losses. This is the particular case when $T_f = 220$ °C, where Q_{total} almost doubles in the transition from $\epsilon_{abs} = 0.1$ to $\epsilon_{abs} = 0.4$. This result indicates that emittance is only a critical factor when HTF operating temperatures are on the top range.

4.3. Correlation for heat losses

In order to apply these results to the assessment of real-scale plants, it is needed to model thermal loses in a straightforward way. Despite the azimuthal distribution of temperature in conventional absorbers and the complex nature of the underlying heat transfer phenomena, reference studies [1] usually select the average absorber temperature $\overline{T}_{abs}$ as the key independent variable which determines total heat losses. In line with this, it has also been suggested to use the difference between the average absorber temperature and the ambient temperature instead, $\Delta T = \overline{T}_{abs} - T_{amb}$. This is the case of another study [45], which experimentally characterized the SCHOTT PTR-70-DSG thermal losses in a real facility. Following the same approach, total heat losses Q_{total} have been plotted vs. ΔT in Fig. 13. It has been presented this way, regardless of the value of the HTF temperature (T_f) or the heat transfer coefficient in the duct h_f.

It has been observed that the polynomial fitting used for conventional receivers also fits the HorseShoe results. The two-parameters function model $Q_{total} = a\Delta T + c\Delta T^4$ has been initially used. As detailed in Table 6, the fitted parameters are close to the values provided for the conventional receiver PTR-70-DSG [45]. However, since thermal radiation losses are dominant, a third parameter is advisable if ΔT is used as the independent variable of the correlation. For that purpose the three-parameter function model $Q_{total} = a\Delta T + b\Delta T^3 + c\Delta T^4$ has also been fitted, showing a higher correlation factor ($R^2 = 0.9996$) in comparison with the two-parameter function model (see Table 6).

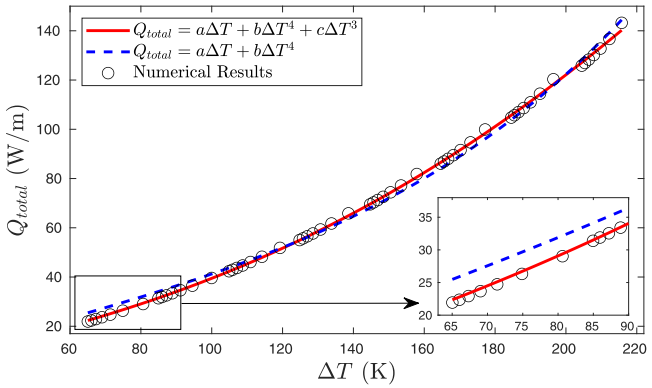

Fig. 13. Total heat losses Q_{total} as a function of the temperature difference between the ambient temperature and the mean temperature of the inner absorber surface ΔT. Two polynomial fittings have been applied (see Table 6).

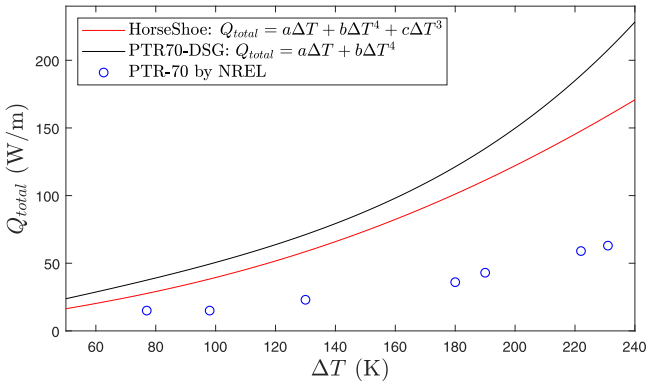

Fig. 14. Comparison of the Total heat losses Q_{total} between the PTR-70 receiver and the HorseShoe design.

Table 6
Parameters of the fitted models to predict heat losses from the temperature difference ΔT.

Function model	Fitting parameters			R^2
	a W/(m K)	b W/(m K^3)	c W/(m K^4)	
Current model				
$a\Delta T + b\Delta T^3 c\Delta T^4$	0.30282	$1.0677 \cdot 10^{-5}$	$-1.4912 \cdot 10^{-8}$	0.9996
$a\Delta T + c\Delta T^4$	0.38407	–	$2.8429 \cdot 10^{-8}$	0.9962
PTR-70-DSG [45]				
$a\Delta T + c\Delta T^4$	0.47123	–	$3.47180 \cdot 10^{-8}$	0.9937

4.4. Comparison with the UVAC receiver

In order to put in context the thermal losses of the HorseShoe design in contrast with the UVAC receiver, the experimental heat losses measured by Burkholder & Kutscher [1] from NREL have been displayed in Fig. 14. Note that the selected range of values for ΔT in this figure have been restricted to operating temperatures suitable to heat for industrial processes. Burkholder & Kutscher carried out experimental characterization in test bed of two PTR-70 receivers. The six experimental points within the considered temperature range indicate relatively low thermal losses. However, in-site experimental results on already-installed PTR-70-DSG receivers [45], suggest that their thermal performance may decay after being operating for two years and a half (see polynomial fitting of the PTR-70-DSG receiver in Table 6 and Fig. 14). This phenomenon may be the direct consequence of the durability limitations pointed out in the introduction. The numerical thermal losses of the HorseShoe receiver are between the two aforementioned PTR-70 curves (see red line). This is relevant, since without having the aforementioned critical elements (i.e. vacuum annulus, expansion bellows or high performance selective coating, which are responsible for the performance drop), the HorseShoe receiver is capable of operating with a relatively similar thermal performance than the UVAC receiver for $T_f < 220$ °C even using a relatively low performance coating (i.e. $\epsilon_{abs} = 0.3$) and keeping their performance stable along his entire lifespan. However, it is also important to note that these are only numerical results and the experimental characterization of the HorseShoe receiver is needed to guarantee the feasibility of the proposed design. Among other reasons, this study is intended to be an initial numerical assessment to check if a further experimental study is justified. These results simply show that despite having considered a more robust concept of receiver and not having sought an extremely efficient design, thermal losses may be at least on the order (or even lower) than an already installed UVAC receiver for the selected range of temperature.

The thermal losses studied correspond to the convective and radiative mechanisms through the slit, so it is expected that the experimental losses are higher than the numerical values provided in this study. It will also be important to consider losses of three-dimensional nature, such as the end-collectors effects, opaque insulation or the bracket supports. On the other hand, although the design proposed in this work solves different technical problems related to the UVAC receiver, it should be noted that the HorseShoe receiver poses some technical challenges, not related to durability but to the manufacturing complexity of the symmetrical lenses. However, some techniques already existing for several decades, such as glass extrusion [46,47], have made it possible to manufacture glass ducts of arbitrary geometry. This technique, in particular, may be suitable for implementing the lenses of the HorseShoe design due to its 2D pattern. In addition, new additive manufacturing techniques [48], along with economy of scale could provide satisfactory results at affordable costs. The cleaning procedure of the lenses may also imply added difficulties during maintenance operations. Initially, this geometry is less vulnerable to soiling, as not all radiation has to cross through the lenses. In line with this, the bottom part of the glass envelope in UVAC receivers is particularly vulnerable because it tends to accumulate more easily dirt dissolved in rain drops. It mainly happens due to their lower slope. This design is less vulnerable to this sort of fouling factor, since all sections of the glass contour have a considerable slope. However, the extra complexity in the process of cleaning the inner face of the lens is still a drawback to be considered.

5. Conclusions

An innovative solar linear receiver based on an open cavity is proposed in this work and studied numerically with an own developed tool. The particular design has been engineered for a primary reflector with the same aperture width as the LS3 reference $W_{LS3} = 5.76/2$ m. For the evaluation of the thermal losses (radiative and convective), a numerical code based on the `chtMultiRegionFoam` with nonstandard boundary conditions has been implemented in OpenFOAM® following a transient Finite Volume Method. The temperature distribution has been obtained for both, solid and fluid domain (air, compressible fluid). In order to get a realistic distribution of the metal absorber temperature, Robin boundary conditions have been used between the Heat Transfer Fluid (HTF) duct and the absorber by means of the corresponding heat transfer coefficient h_f.

It has been found that due to the fluctuating nature of the thermal plume, a transient solver is recommended in order to properly track heat losses due to natural convection. However, not convection, but thermal radiation is responsible for most of the heat losses. It can be explained by the stratification of the air inside the cavity, which is

enhanced by the pair of symmetric lenses. Provided that HTF temperature is within the range from T_f = 80 °C to T_f = 220 °C and the duct heat transfer coefficient h_f ranges from h_f = 600 W/(m^2 K) to h_f = 1800 W/(m^2 K), numerical thermal performance is higher than $\eta_{thermal} > 0.96$ when the emittance of the active surface of the absorber is set at $\epsilon_{abs} = 0.3$. The value provided for $\eta_{thermal}$ accounts for the 2D thermal losses due to convection and thermal radiation through the slit as the most significant and complex heat transfer phenomenon limiting the global performance. It is also important to highlight that h_f plays a key role in the absorber temperature distribution, whereas T_f is the variable having a more relevant influence on the total heat losses Q_{loss}. In fact, heat losses are virtually independent of h_f when $h_f > 1400$ W/(m^2 K).

The temperature difference between the coldest and hottest points in the absorber is crucial in order to assess the receiver technical viability. Under the aforementioned conditions, this temperature difference has been found to be upper bounded by 30 K, which indicates that the proposed design is feasible. However, there is still leeway to reduce such temperature gradients by modifying the metal absorber geometry, e.g. increasing the wet perimeter. This optimization task can be accomplished without having to modify the slit width d.

Finally, a polynomial correlation for the total heat losses vs. the difference between the mean temperature of the active surface of the absorber and the ambient temperature has been proposed. It shows that these correlation parameters are on the order of those experimentally obtained by the PTR-70 receiver. After this comparison, numerical results suggest that a further experimental test is justified.

Nomenclature

A Area per unit length (m)
F_{i-j} View factor between surface i and j (–)
Gr Grashof number (–)
K Kinetic Energy (J/kg)
L Characteristic length (m)
Pr Prandtl number (–)
Q_{total} Total heat losses (W/m)
R Correlation coefficient (–)
Re Reynolds number (–)
T Temperature (K, °C)
W Collector width (m)
$\mathbf{B}$ Column vector
$\mathbf{C}$ Square matrix
$\mathbf{g}$ Gravitational acceleration (m/s^2)
$\mathbf{n}$ Normal unit vector (m)
$\mathbf{v}$ Velocity vector (m/s)
a Heat loss correlation parameter [W/(m K)], Parameter of the modified reflector (m)
b Heat loss correlation parameter [W/(m K^4)]
c Heat loss correlation parameter [W/(m K^3)]
$c_{p,abs}$ Specific heat capacity at constant pressure [J/(kg K)]
d Width of the cavity slit (m)
e Internal energy (J/kg)
f Focal distance (m)
h Solid enthalpy (J/kg)
h_f Heat transfer coefficient [W/(m^2 K)]
h_l Local heat transfer coefficient [W/(m^2 K)]
p Pressure (N/m^2)
q Heat flux (W/m^2)
q_f Heat flux on the fluid (W/m^2)
q_{rad} Heat flux from thermal radiation (W/m^2)
q_{sun} Heat flux from solar radiation (W/m^2)
q_s Heat flux on the solid (W/m^2)
r Additional heat flux (W/m^2)
t Time (s)
x Horizontal coordinate (m)
x_{trans} Transition length in the reflector profile (m)
y Vertical coordinate (m)

Abbreviations

CFD Computational Fluid Dynamics
CFL Courant–Friedrichs–Lewy
CSP Concentrated Solar Power
DNI Direct Normal Irradiance
EOS Equation of State
HTF Heat Transfer Fluid
LCOE Levelized Cost Of Energy
LCR Local Concentration Ratio
O&M Operation and Maintenance
PTC Parabolic Trough Collector
UVAC Universal Vacuum Air Collector

Greek Symbols

α Effective thermal diffusivity [kg/(m s)]
β Coefficient of thermal expansion (K^{-1})
ΔT Temperature difference (K)
δ Parameter of the modified reflector profile (–)
δ_{ij} Kronecker's delta
ϵ Emittance of a surface (–)
η Efficiency (–)
κ Thermal conductivity [W/(m K)]
μ Dynamic viscosity of air (N s/m^2)
ρ Density (kg/m^3)
σ Stephan–Boltzmann's constant
Σ_n Patch n in the computational domain
τ Viscous stress tensor (N/m^2)
θ Angle defining the HorseShoe cavity (rad)
ε Relative error (–)
ξ_{rad} Thermal radiation factor (–)

Subscripts

$0-7$ Patch numeration
abs Absorber
amb Ambient
f Fluid flow domain
i, j Surface indexes
$LS3$ Relative so the LS3 trough design
max Maximum
min Minimum
mod Modified design of reflector
$N \times 1$ Size of column vector
$N \times N$ Size of square matrix
rad Thermal radiation
s Steel absorber domain
src Source
sun Solar radiation
$surr$ Absorber surrounding surfaces
$thermal$ Thermal

Declaration of competing interest

The authors declare the following financial interests/personal relationships which may be considered as potential competing interests: J.J. Serrano-Aguilera and L Parras are inventors of an invention ("Linear-focus solar collector with a horseshoe-shaped open receiver") related to the results included in this work, said invention being the

object of the spanish patent ES2844999B2 and the international PCT application WO2021148701A1.

Data availability

No data was used for the research described in the article.

Acknowledgments

Second (corresponding) author J.J. Serrano-Aguilera acknowledges the support provided by Junta de Andalucía (Government of Andalusia) and Universidad de Málaga for the source of funding for the HERTERSOL project (UMA18-FEDERJA-195), as well as to Ministerio de Ciencia, Innovación *y* Universidades (Spain) by means of the post-doc position: Ref No. FJCI-2017-32403 (Juan de la Cierva-Formación Postdoc Grant). Third author acknowledges the support of Universidad de Málaga, Spain through the Project WALICON, 2021. Authors also acknowledge funding for open access charge: Universidad de Málaga / CBUA.

Appendix A. Supplementary data

Supplementary material related to this article can be found online at https://doi.org/10.1016/j.applthermaleng.2022.118949. Supplementary material associated with this article consists of one video showing the transient evolution of the thermal plume above the receiver.

References

[1] F. Burkholder, C. Kutscher, Heat-Loss Testing of Solel's UVAC3 Parabolic Trough Receiver, Technical Report NREL/TP-550-42394, Tech. rep., National Renewable Energy Laboratory, 2008.

[2] Sargent & Lundy LLC Consulting Group Chicago, Illinois, Assessment of Parabolic Trough and Power Tower Solar Technology Cost and Performance Forecasts, Subcontract Report NREL/SR-550-34440, Tech. rep., National Renewable Energy Laboratory, 2003.

[3] C. Raggi, T. Chiarappa, A glass-to-metal joint for a solar receiver, 2013, European Patent 2626336 A1.

[4] A. Morales, G. San Vicente, A new generation of absorber tubes for concentrating solar thermal (CST) systems, in: M.J. Blanco, L.R. Santigosa (Eds.), Advances in Concentrating Solar Thermal Research and Technology, in: Woodhead Publishing Series in Energy, Woodhead Publishing, 2017, pp. 59–73, http://dx.doi.org/10.1016/B978-0-08-100516-3.00004-6.

[5] J. Liu, D. Lei, Q. Li, Vacuum lifetime and residual gas analysis of parabolic trough receiver, Renew. Energy 86 (2016) 949–954, http://dx.doi.org/10.1016/j.renene.2015.08.065.

[6] H. Cachafeiro, L.F. de Arevalo, R. Vinuesa, J. Goikoetxea, J. Barriga, Impact of solar selective coating ageing on energy cost, Energy Procedia 69 (2015) 299–309, http://dx.doi.org/10.1016/j.egypro.2015.03.034, International Conference on Concentrating Solar Power and Chemical Energy Systems, SolarPACES 2014.

[7] Guillermo Espinosa-Rueda, José Luis Navarro Hermoso, Noelia Martínez-Sanz, Manuel Gallas-Torreira, Degradation of receiver tube optical performance after four years of operation, Sol. Energy 135 (2016) 122–129, http://dx.doi.org/10.1016/j.solener.2016.05.034.

[8] L. Li, J. Sun, Y. Li, Thermal load and bending analysis of heat collection element of direct-steam-generation parabolic-trough solar power plant, Appl. Therm. Eng. 127 (2017) 1530–1542, http://dx.doi.org/10.1016/j.applthermaleng.2017.08.129.

[9] Renewable Power Generation Costs in 2019. ISBN 978-92-9260-244-4, Tech. rep., International Renewable Energy Agency, Abu Dhabi, 2020.

[10] H. Cachafeiro, L.F. de Arevalo, R. Vinuesa, R. Lopez-Vizcaino, M. Luna, Analysis of vacuum evolution inside solar receiver tubes, Energy Procedia 69 (2015) 289–298, http://dx.doi.org/10.1016/j.egypro.2015.03.033, International Conference on Concentrating Solar Power and Chemical Energy Systems, SolarPACES 2014.

[11] J.D. Osorio, A. Rivera-Alvarez, Performance analysis of parabolic trough collectors with double glass envelope, Renew. Energy 130 (2019) 1092–1107, http://dx.doi.org/10.1016/j.renene.2018.06.024.

[12] M.A. Janan, M. Taqi, H. Chakir, Impact of gas-filled annular space on thermal and optical performances of a heat pipe parabolic trough solar collector, J. Solar Energy Eng. 143 (6) (2021) http://dx.doi.org/10.1115/1.4050709, 061001.

[13] R.G. Patil, S.V. Panse, J.B. Joshi, V.H. Dalvi, Alternative designs of evacuated receiver for parabolic trough collector, Energy 155 (2018) 66–76, http://dx.doi.org/10.1016/j.energy.2018.05.022.

[14] M.M. El-Bakry, M.A. Kassem, M.A. Hassan, Passive performance enhancement of parabolic trough solar concentrators using internal radiation heat shields, Renew. Energy 165 (2021) 52–66, http://dx.doi.org/10.1016/j.renene.2020.11.003.

[15] S.-Y. Wu, L. Xiao, Y. Cao, Y.-R. Li, Convection heat loss from cavity receiver in parabolic dish solar thermal power system: A review, Sol. Energy 84 (8) (2010) 1342–1355, http://dx.doi.org/10.1016/j.solener.2010.04.008.

[16] D. Azzouzi, B. Boumeddane, A. Abene, Experimental and analytical thermal analysis of cylindrical cavity receiver for solar dish, Renew. Energy 106 (2017) 111–121, http://dx.doi.org/10.1016/j.renene.2016.12.102.

[17] H. Chang, C. Duan, K. Wen, Y. Liu, C. Xiang, Z. Wan, S. He, C. Jing, S. Shu, Modeling study on the thermal performance of a modified cavity receiver with glass window and secondary reflector, Energy Convers. Manage. 106 (2015) 1362–1369, http://dx.doi.org/10.1016/j.enconman.2015.10.043.

[18] F. Cui, Y. He, Z. Cheng, Y. Li, Study on combined heat loss of a dish receiver with quartz glass cover, Appl. Energy 112 (2013) 690–696, http://dx.doi.org/10.1016/j.apenergy.2013.01.007.

[19] P. Schöttl, G. Bern, D.W. van Rooyen, J.A. Fernández Pretel, T. Fluri, P. Nitz, Optimization of solar tower molten salt cavity receivers for maximum yield based on annual performance assessment, Sol. Energy 199 (2020) 278–294, http://dx.doi.org/10.1016/j.solener.2020.02.007.

[20] O. Barra, L. Franceschi, The parabolic trough plants using black body receivers: Experimental and theoretical analyses, Sol. Energy 28 (2) (1982) 163–171, http://dx.doi.org/10.1016/0038-092X(82)90295-X.

[21] A. Rafiei, R. Loni, M.H. Ahmadi, G. Najafi, E. Bellos, F. Rajaee, E. Askari Asli-Ardeh, Sensitivity analysis of a parabolic trough concentrator with linear V-shape cavity, Energy Sci. Eng. 8 (10) (2020) 3544–3560, http://dx.doi.org/10.1002/ese3.763.

[22] H. Zhai, Y. Dai, J. Wu, R. Wang, Energy and exergy analyses on a novel hybrid solar heating, cooling and power generation system for remote areas, Appl. Energy 86 (9) (2009) 1395–1404, http://dx.doi.org/10.1016/j.apenergy.2008.11.020.

[23] R. Loni, B. Ghobadian, A. Kasaeian, M. Akhlaghi, E. Bellos, G. Najafi, Sensitivity analysis of parabolic trough concentrator using rectangular cavity receiver, Appl. Therm. Eng. 169 (2020) 114948, http://dx.doi.org/10.1016/j.applthermaleng.2020.114948.

[24] F. Chen, M. Li, P. Zhang, X. Luo, Thermal performance of a novel linear cavity absorber for parabolic trough solar concentrator, Energy Convers. Manage. 90 (2015) 292–299, http://dx.doi.org/10.1016/j.enconman.2014.11.034.

[25] X. Xiao, P. Zhang, D. Shao, M. Li, Experimental and numerical heat transfer analysis of a V-cavity absorber for linear parabolic trough solar collector, Energy Convers. Manage. 86 (2014) 49–59, http://dx.doi.org/10.1016/j.enconman.2014.05.001.

[26] X. Li, H. Chang, C. Duan, Y. Zheng, S. Shu, Thermal performance analysis of a novel linear cavity receiver for parabolic trough solar collectors, Appl. Energy 237 (2019) 431–439, http://dx.doi.org/10.1016/j.apenergy.2019.01.014.

[27] J. Serrano-Aguilera, L. Valenzuela, L. Parras, Thermal 3D model for direct solar steam generation under superheated conditions, Appl. Energy 132 (2014) 370–382, http://dx.doi.org/10.1016/j.apenergy.2014.07.035.

[28] J. Serrano-Aguilera, L. Valenzuela, J. Fernández-Reche, Inverse Monte Carlo Ray-tracing method (IMCRT) applied to line-focus reflectors, Sol. Energy 124 (2016) 184–197, http://dx.doi.org/10.1016/j.solener.2015.11.036.

[29] OpenFOAM®: Open source CFD: Documentation, 2021, www.openfoam.com/documentation/guides/latest/doc/, Accessed: 2021-08-31.

[30] M.F. Modest, Chapter 5 - radiative exchange between gray, diffuse surfaces, in: Radiative Heat Transfer, Academic Press, Boston, 2013, pp. 160–196.

[31] H.G. Weller, G. Tabor, H. Jasak, C. Fureby, A tensorial approach to computational continuum mechanics using object-oriented techniques, Comput. Phys. 12 (6) (1998) 620–631.

[32] G. Krishnendu, J. Jayakumar, CFD analysis of combined thermal radiation and conjugate heat transfer in a 3D FFS, in: Materials, Design, and Manufacturing for Sustainable Environment, Springer, 2021, pp. 835–850.

[33] Z. Lin, A.A. Al-Shabab, D. Vitlaris, P. Tsoutsanis, A. Antoniadis, M. Skote, Effects of heat-conductive obstacles on conjugate heat transfer of backward-facing step flow, in: AIAA Scitech 2021 Forum, 2021, p. 2007.

[34] S. Sandler, B. Zajaczkowski, B. Bialko, Z.M. Malecha, Evaluation of the impact of the thermal shunt effect on the U-pipe ground borehole heat exchanger performance, Geothermics 65 (2017) 244–254.

[35] J.H. Ferziger, M. Perić, R.L. Street, Computational Methods for Fluid Dynamics, Vol. 3, Springer, 2002.

[36] M. Khatamifar, W. Lin, L. Dong, Transient conjugate natural convection heat transfer in a differentially-heated square cavity with a partition of finite thickness and thermal conductivity, Case Stud. Therm. Eng. 25 (2021) 100952, http://dx.doi.org/10.1016/j.csite.2021.100952.

[37] K. Lampio, R. Karvinen, Optimization of convectively cooled heat sinks, Microelectron. Reliab. 79 (2017) 473–479, http://dx.doi.org/10.1016/j.microrel.2017.06.011.

[38] Z.H. Che Daud, D. Chrenko, F. Dos Santos, E.-H. Aglzim, A. Keromnes, L. Le Moyne, 3D electro-thermal modelling and experimental validation of lithium polymer-based batteries for automotive applications, Int. J. Energy Res. 40 (8) (2016) 1144–1154, http://dx.doi.org/10.1002/er.3524, arXiv:https://onlinelibrary.wiley.com/doi/pdf/10.1002/er.3524.

[39] P. Renze, K. Akermann, Simulation of conjugate heat transfer in thermal processes with open source CFD, ChemEngineering 3 (2) (2019) http://dx.doi.org/10.3390/chemengineering3020059.
[40] G. Brösigke, A. Herter, M. Rädle, J.-U. Repke, Direct numerical simulation of conjugated heat transfer between a spherical particle rolling over a planar surface, Appl. Therm. Eng. 139 (2018) 456–463, http://dx.doi.org/10.1016/j.applthermaleng.2018.05.007.
[41] D. Angirasa, M.J.B.M. Pourquié, F.T.M. Nieuwstadt, Numerical study of transient and steady laminar buoyancy-driven flows and heat transfer in a square open cavity, Numer. Heat Transfer A 22 (2) (1992) 223–239, http://dx.doi.org/10.1080/10407789208944766.
[42] V. Sernas, I. Kyriakides, Natural convection in an open cavity, in: Proceedings of the Seventh International Hear Transfer Conference, Munich, Vol. 2, 1982, pp. 275–286.
[43] Y. Chan, C. Tien, A numerical study of two-dimensional natural convection in square open cavities, Numer. Heat Transfer 8 (1) (1985) 65–80, http://dx.doi.org/10.1080/01495728508961842.
[44] W. Chakroun, M.M. Elsayed, S.F. Al-Fahed, Experimental measurements of heat transfer coefficient in a partially/fully opened tilted cavity, J. Solar Energy Eng. 119 (4) (1997) 298–303, http://dx.doi.org/10.1115/1.2888036.
[45] J. Serrano-Aguilera, L. Valenzuela, L. Parras, Thermal hydraulic RELAP5 model for a solar direct steam generation system based on parabolic trough collectors operating in once-through mode, Energy 133 (2017) 796–807, http://dx.doi.org/10.1016/j.energy.2017.05.156.
[46] E. Roeder, Extrusion of glass, J. Non-Cryst. Solids 5 (5) (1971) 377–388, http://dx.doi.org/10.1016/0022-3093(71)90039-1.
[47] E. Minay, V. Desbois, A. Boccaccini, Innovative manufacturing technique for glass matrix composites: extrusion of recycled TV set screen glass reinforced with al2o3 platelets, J. Mater. Process. Technol. 142 (2) (2003) 471–478, http://dx.doi.org/10.1016/S0924-0136(03)00644-7.
[48] J. Klein, M. Stern, G. Franchin, M. Kayser, C. Inamura, S. Dave, J. Weaver, P. Houk, P. Colombo, M. Yang, N. Oxman, Additive manufacturing of optically transparent glass, 3D Print. Addit. Manuf. 2 (3) (2015) 92–105, http://dx.doi.org/10.1089/3dp.2015.0021.